

SORCE-SOLSTICE Release Notes for Version 17, Level 3 data products

J.P. Elliott, M. Snow, B. Vanier, J. Mothersbaugh, E. Lieb
Laboratory for Atmospheric and Space Physics, University of Colorado

SOLSTICE data Version 17 (V17) appears in three locations:

1. On the LISIRD website: <http://lasp.colorado.edu/lisird/sorce/>
2. On the SORCE website: <http://lasp.colorado.edu/home/sorce/data/>
3. On the NASA DAAC:
FUV: https://disc.gsfc.nasa.gov/datasets/SOR3SOLFUV_017/summary
MUV: https://disc.gsfc.nasa.gov/datasets/SOR3SOLMUV_017/summary

Table 1 below gives a description of available time and wavelength ranges for each location.

An IDL reader for the ASCII formatted data present on the SORCE web site is available at: http://lasp.colorado.edu/data/sorce/file_readers/read_lasp_ascii_file.pro

Time Range	Wavelength Range (nm)	
04/14/2003 - present	. 115 - 180	.180 - 310
	. FUV .	. MUV

Table 1: Time and wavelength ranges for each repository location.

Calibration Changes:

V17 of SORCE SOLSTICE employs the same correction algorithms as V17 with the following changes:

I. Field-of-View (FOV) degradation correction.

An updated field-of-view (FOV) degradation correction was applied to the MUV channel on SOLSTICE B. Earlier in the mission this correction relied upon a cruciform alignment “haystack” scan which we performed at 8 discrete wavelengths. The center minimum in the haystack occurs at the center of the detector where daily irradiance measurements are made. The two peaks, or “shoulders”, occur at the edges of the detector and are not exposed as often and are therefore less degraded. We take the ratio of the center value to the mean of the shoulders to calculate the FOV degradation. Figure 1 below illustrates one such scan.

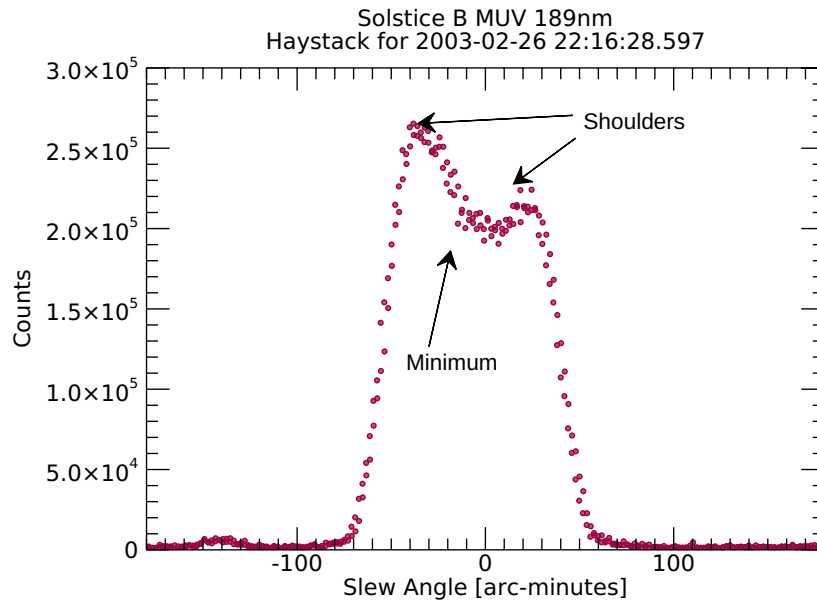


Figure 1: Cruciform alignment "haystack" scan at 189nm

However, these cruciform scans significantly under-sampled the wavelength range and therefore did not accurately capture the FOV degradation at all wavelengths. Further, the cruciform scans were no longer performed once the spacecraft entered the day-only-operations mode (DO-Op) of the mission. We instead began special “off-pointing” experiments which scan the entire wavelength range, while reducing the sampling in the slew (pointing) dimension, but still capturing the FOV measurement. These measurements occurred while the spacecraft was off-pointed directly at the shoulder location, and then at the center location. This allowed us to calculate the FOV degradation at a much finer wavelength scale than before (at 1nm intervals). Further, we model and extrapolate this new higher resolution degradation backward in time in order to apply it to the entire mission.

For wavelengths that have both cruciform scan data and off-pointing data, we can fit an exponential decay model for the entire mission and compare to the old haystack degradation model. And for wavelengths which only have off-pointing data but no haystacks, we can extrapolate backward in time. Figure 2 illustrates the two models independently while Figure 3 illustrates the new combined FOV degradation model. Off-pointing (blue points), FOV Model (green surface)

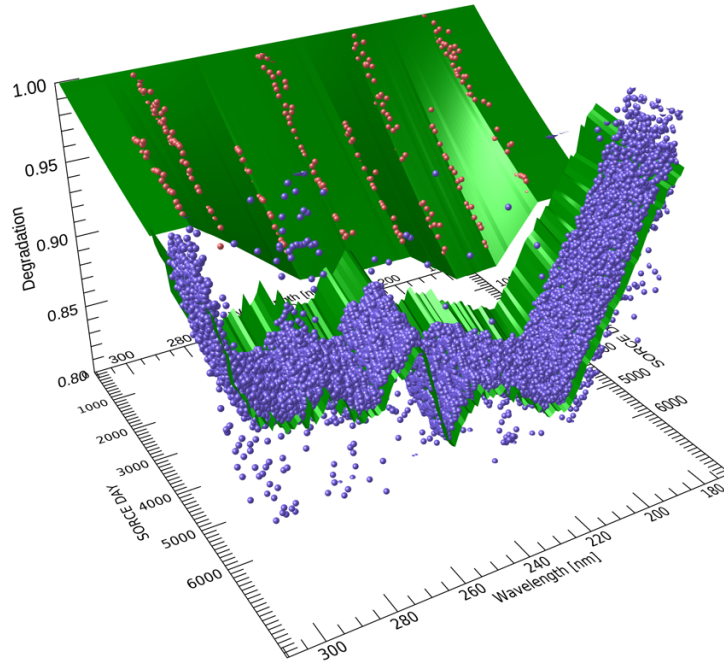


Figure 2: Haystack model (red points), Off-pointing (blue points), FOV Model (green surface)

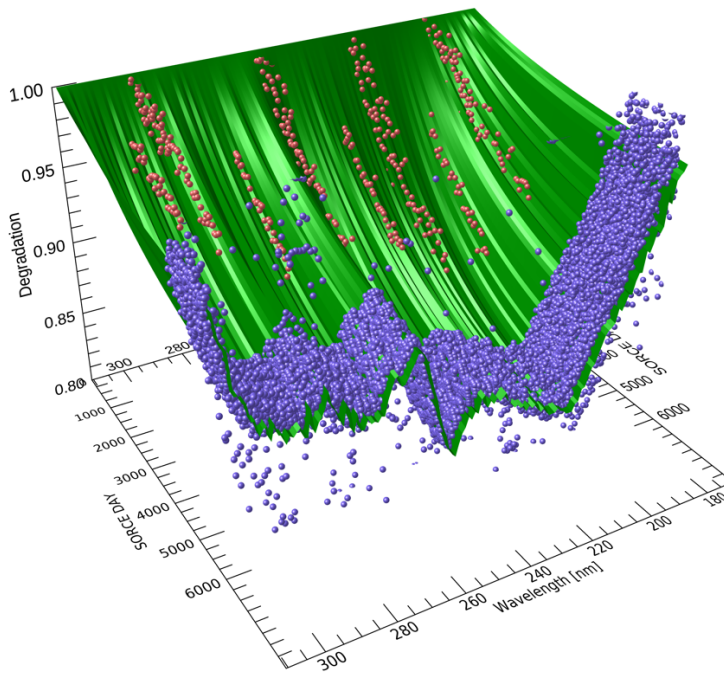


Figure 3: Combined FOV Model

II. Exposure-time based detector degradation.

Separate from the FOV degradation are the effects of detector degradation. Early in the mission this was measured by observing UV bright stars with known spectra in order to calibrate SOLSTICE. However, later in the mission (DO-Op) it was no longer possible to make stellar measurements, and so we had been extrapolating that earlier degradation model into DO-Op. However, due to operational changes we take MUV measurements on SOLSTICE B much more frequently in DO-Op than in the early part of the mission, and therefore are exposing the MUV detector much more than before. To account for this, we take the cumulative counts collected

over the life of the mission to get an estimate of the equivalent “exposure days” as a function of “mission days”. In addition, a pointing analysis was performed which showed that on each orbit prior to the beginning of an observation while the spacecraft was acquiring the sun, the detector can become illuminated which further degrades the detector. This additional exposure was also added to this exposure-time based model.

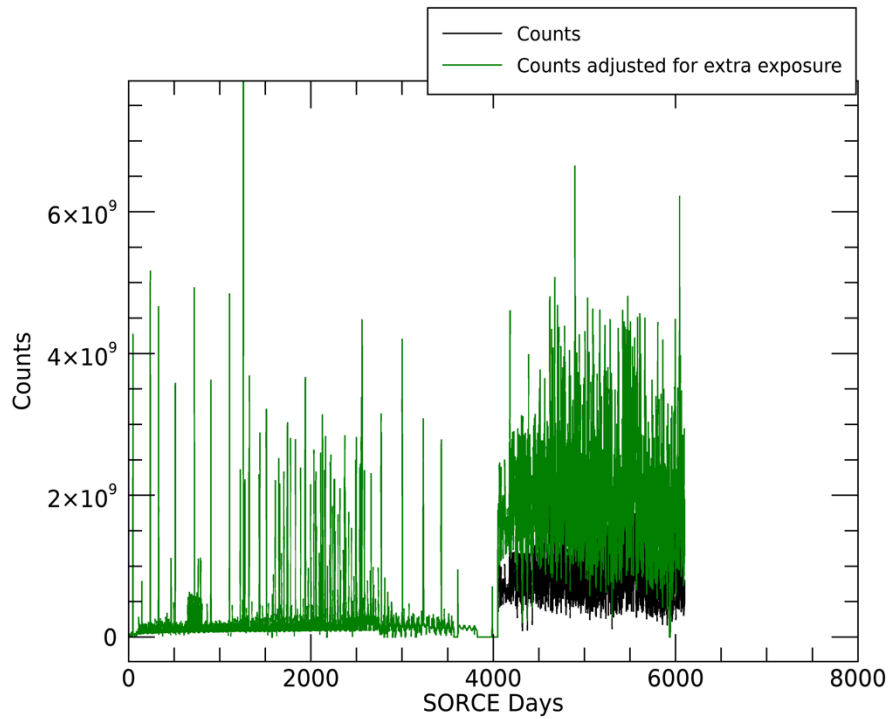


Figure 4: Counts adjusted for extra exposure time.

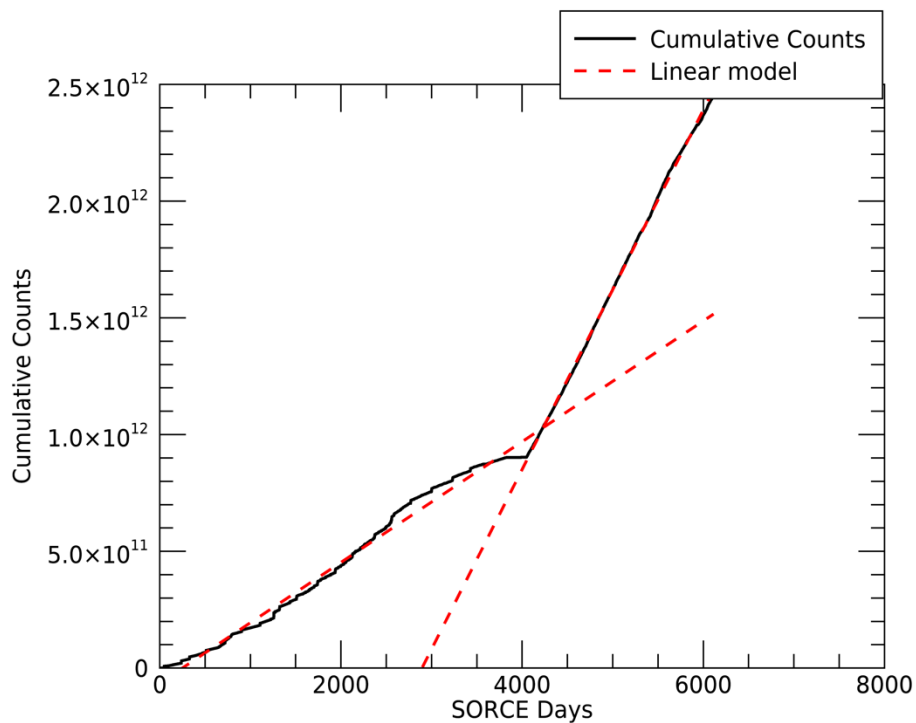


Figure 5: Cumulative Counts

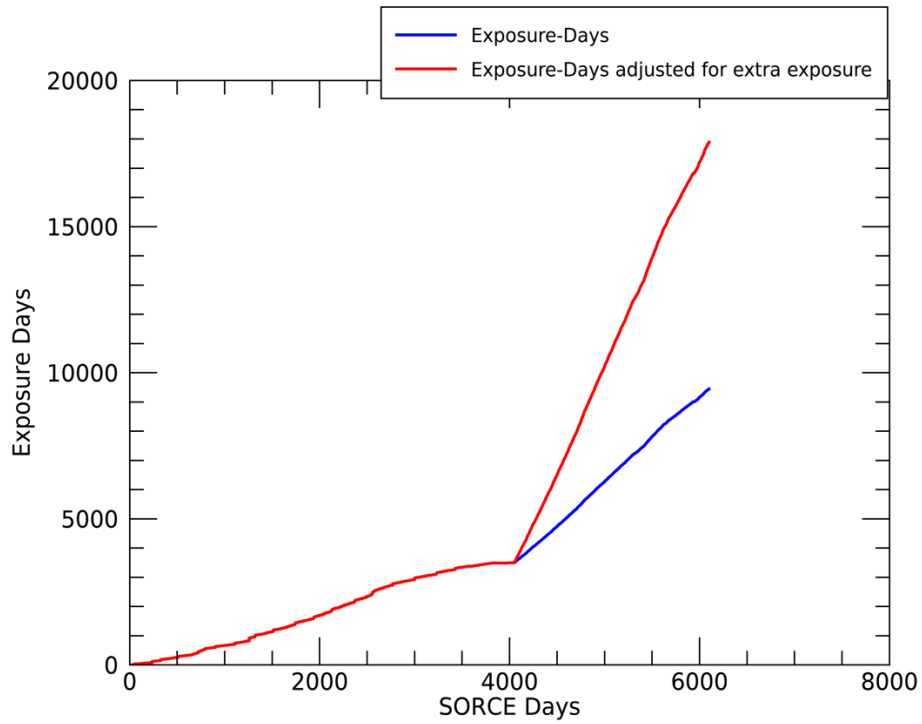


Figure 6: Exposure Day model.

III. Solar image spot size correction.

We improved the second-order 1AU correction for the SOLSTICE B MUV detector based on the size of the solar image incident on the detector as it changes throughout the year. This is in addition to the usual 1AU normalization correction that is performed. When the solar image is larger the sun illuminates part of the optics with less degradation resulting in an apparent higher sensitivity of the detector. Conversely, when the spacecraft is farther away, the sun's image is smaller and it falls on the less sensitive regions of the optics. To make this correction we integrate the haystack over the nominal size of the sun on the optics at 30 arcminutes.

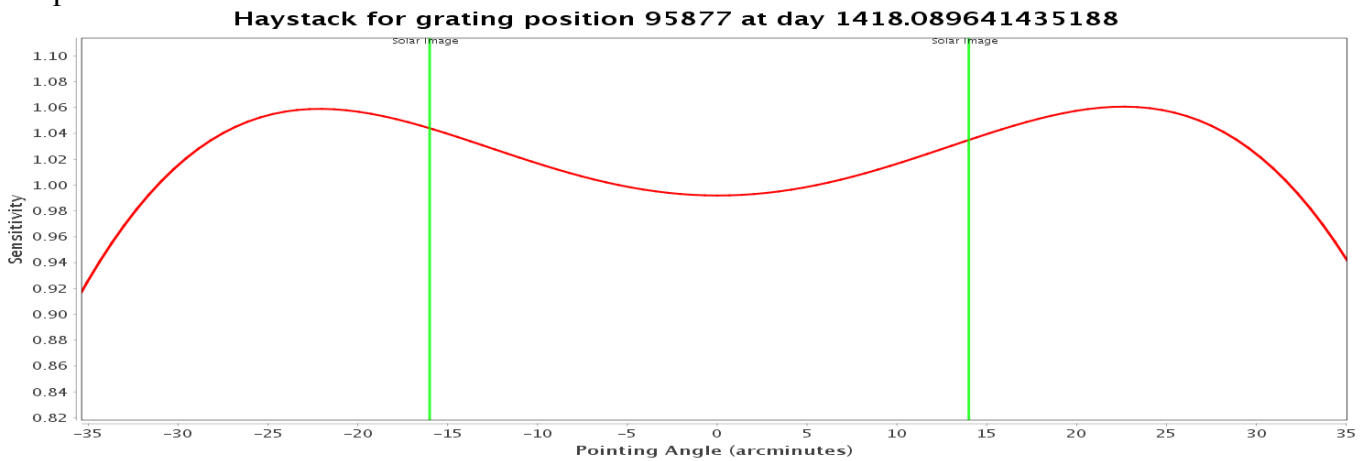


Figure 7: Example haystack with Solar image size boundary over plotted.

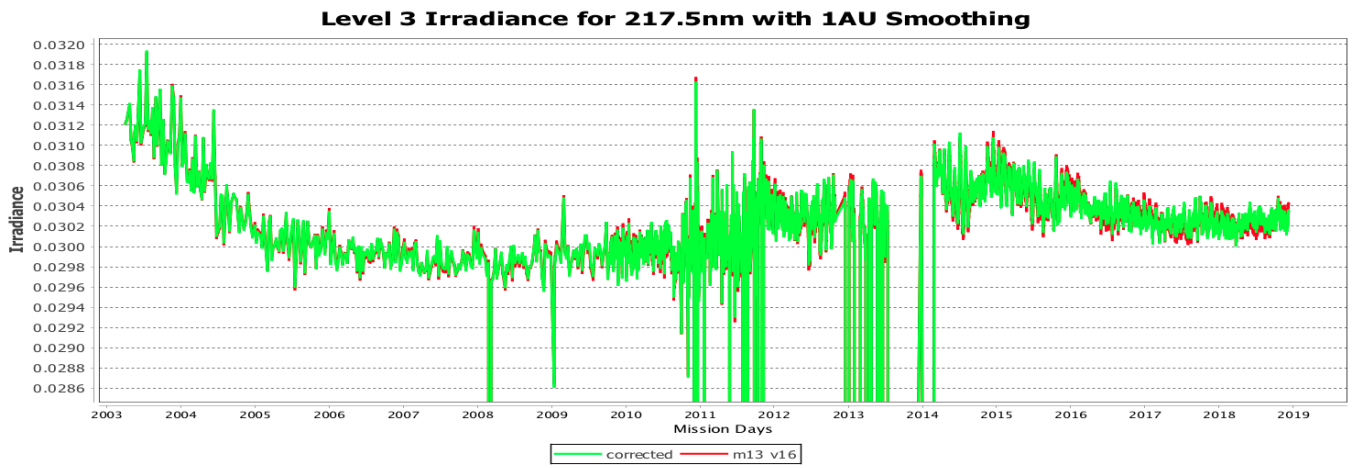


Figure 8: Example time series at 217.5nm showing the spot-size corrected irradiance.

IV. Gain uncertainty calculation.

An improved gain-uncertainty dependent on detector temperature in order to improve our L3 data product uncertainty.

An error was discovered by an external user in the V16 (L3) SOLSTICE irradiance uncertainties. The reported uncertainties in the MUV at long wavelengths were too large and displayed odd time-dependent characteristics. Analysis of the calculation pipeline revealed that the problem with the uncertainties was originating in the code that calculates the temperature gain uncertainties. An incorrect equation, using improperly derived temperature coefficients, was being used to find the temperature gain as a function of wavelength, and the associated uncertainties were also incorrect.

The incorrect temperature gain uncertainties were carried forward through the processing pipeline to the corrected count rate, L2 systematic, L2 combined and ultimately the L3 combined uncertainties. The incorrect uncertainties were present in all modes but were most noticeable in the MUV (modes 9 (SOLSTICEA) and 13 (SOLSTICEB)) detectors.

The new temperature gain uncertainties significantly reduce the uncertainty values and rely only data that is obtained from spacecraft telemetry rather than on the previous model.

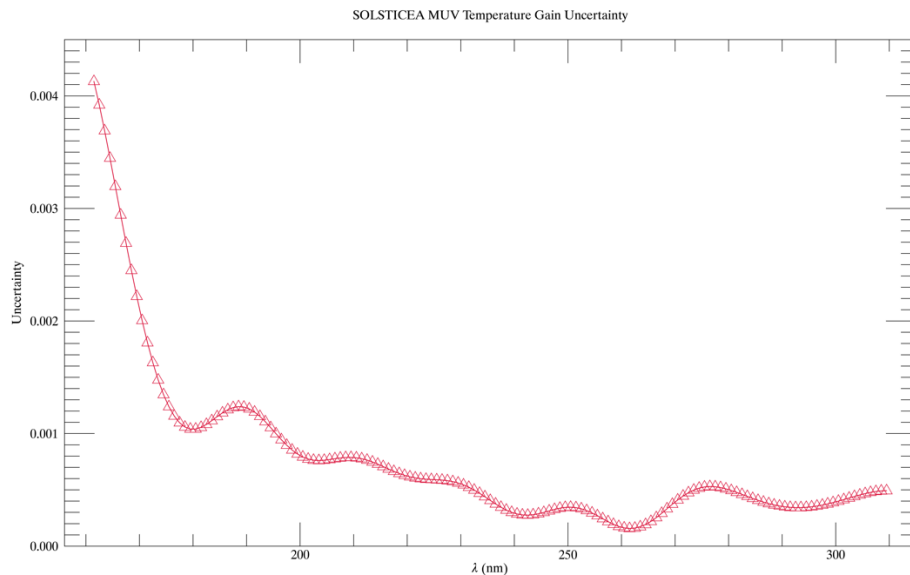


Figure 9: Gain uncertainty as a function of wavelength.

The plot above shows temperature gain uncertainty vs. wavelength, independent of temperature. Each point is the uncertainty of the slope of the fit of temperature gain vs. temperature at that single wavelength.

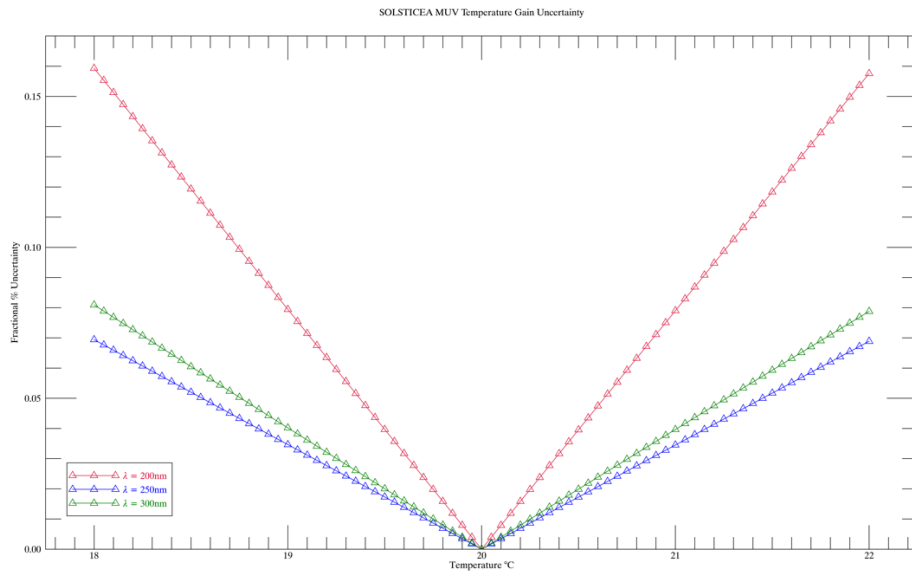


Figure 10: Temperature gain uncertainty as a fractional percentage of temperature gain vs. temperature

This plot shows temperature gain uncertainty as a fractional percentage of temperature gain vs. temperature at 200, 250 and 300nm for SOLSTICEA MUV. A reference grid of temperature values was used in the temperature gain and uncertainty equations described above to generate this plot. In the data processing pipeline, the actual temperature at the time of the scan is used to generate a single gain uncertainty value at each wavelength.

The plots below show the L3 combined irradiance uncertainties as a fractional percentage of the L3 irradiance. Red is V16, blue is V17. The improvement in the uncertainties due to the new temperature gain uncertainty is obvious and significant.

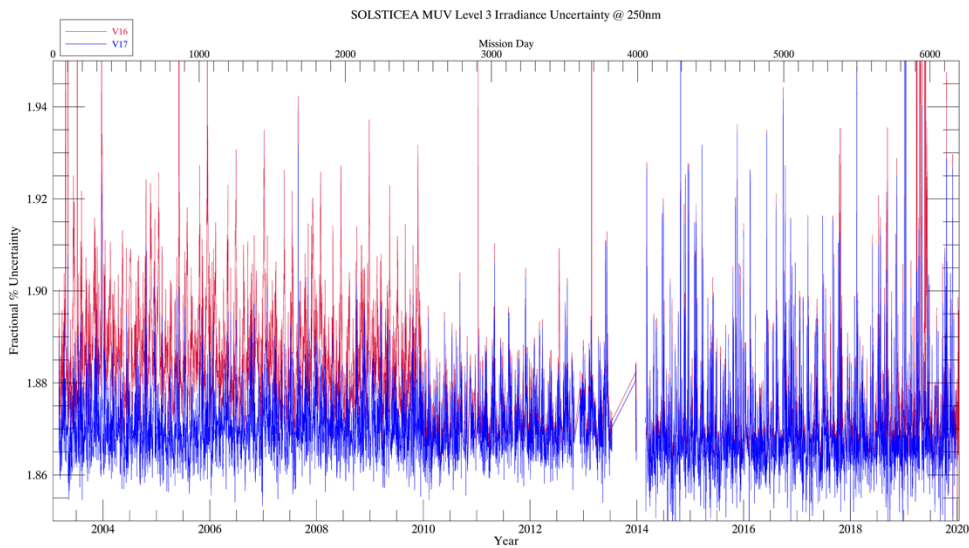


Figure 11: L3 Uncertainty for 250nm

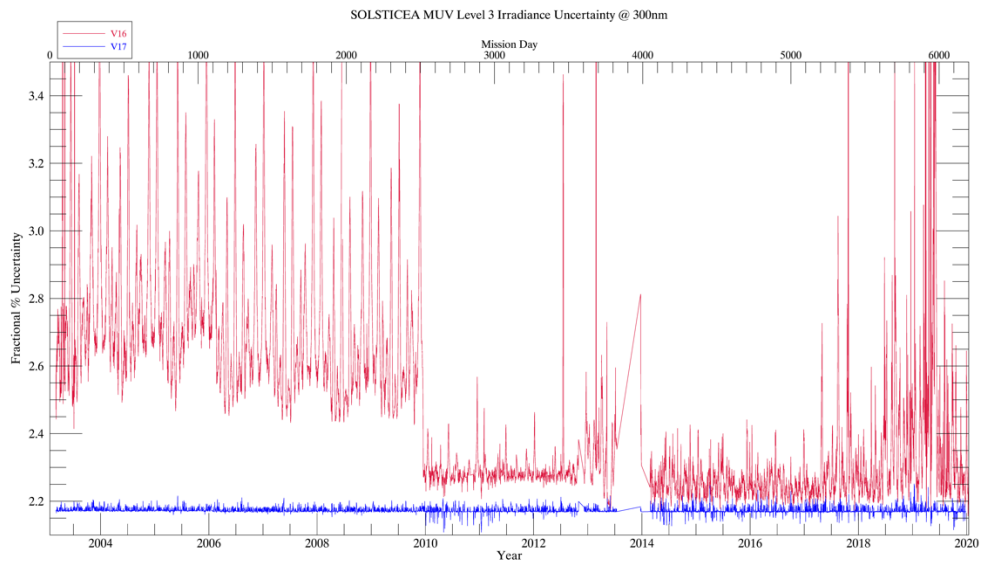


Figure 12:L3 Uncertainty for 300nm